THz pulse generation and real-time THz imaging

Toshiaki Hattori[a], Rakchanok Rungsawang[a], Keiji Tukamoto[a], and Ryuzi Yano[b]

[a]Institute of Applied Physics, University of Tsukuba, 1-1-1 Tennodai, Tsukuba, 305-8573 Japan;
[b]Department of Materials Science and Engineering, Muroran Institute of Technology, 27-1 Mizumoto-cho, Muroran, Hokkaido 050-8585, Japan

ABSTRACT

Terahertz electromagnetic pulse generation using photoconductive emitters, their characterization, real-time imaging, and spectroscopies using them are described. Intense THz pulses were generated using a large-aperture photoconductive antenna. Real-time imaging were performed for the pulse characterization and acquisition of 1-kHz high-speed movies of moving objects. Tunable THz pulse generation and ultrafast semiconductor spectroscopy using photoconductive antennas will also be described.

Keywords: terahertz radiation, half-cycle pulses, photoconductive antenna, ultrafast electron dynamics, GaAs, InP

1. INTRODUCTION

Terahertz (THz) waves are electromagnetic radiation with a frequency ranging from 100 GHz to 10 THz. This frequency region lies at the boundary of radio waves and light in the wide spectrum of the electromagnetic waves. Little studies and uses of THz waves have been done until recent years because of the difficulty in their generation, manipulation, and detection. Recent advances in the solid-state laser technology are accelerating their studies and applications. One of the most promising applications of THz waves is imaging. THz waves can penetrate through nonmetallic and non-polar materials, such as paper, plastics, and textiles. THz waves are much safer than x-rays and can be used for identification of specific chemicals such as drugs. Applications of THz imaging for security check, product inspection, and medical diagnoses are expected. For many of these applications, real-time acquisition of the image data is required. We use intense THz pulses emitted from a large-aperture photoconductive antenna for the real-time THz imaging.[1–5]

We first describe the technique of real-time THz imaging using a large-aperture emitter, two-dimensional electro-optic (EO) sampling, and an image detector in Sect. 2. Then characterization of the THz pulses in the time and spatial domains will be described in Sect. 3. The technique to enhance the image acquisition rate up to 1 kHz and some results on high-speed movie acquisition of a moving object will be described in Sect. 4. In Sect. 5, a technique that enables generation of tunable phase-stable narrow-band THz pulses will be described. Finally, in Sect. 6, we will describe a THz spectroscopic study of ultrafast electron dynamics in semiconductors.

2. REAL-TIME THZ IMAGING

Here, we will describe the technique of real-time THz imaging using intense THz pulses and a two-dimensional EO sampling method. The applications of the technique to the characterization of the THz pulses and high-speed movies will be given in Sects. 3, and 4, respectively.

For various real-world application of THz imaging, real-time acquisition and processing of the image data is requisite. We use intense THz pulses obtained from a large-aperture emitter for the real-time acquisition of THz images. The peak electric field of the focused THz pulse can reach up to 20 kV/cm Imaging without scanning the position of the THz beam or the sample becomes possible using the intense THz pulses. A schematic of a typical experimental setup of the real-time THz imaging using a large-aperture emitter is shown in Fig. 1.[1–5] The emitter is made of a semi-insulating GaAs wafer with two electrodes. The spacing between the electrodes is 30 mm, and a high voltage of about 10 kV is applied. The emitter is pumped by amplified 130-fs, 800-nm pulses at a repetition rate of 1 kHz. For imaging of objects, the sample is placed close to the emitter. The

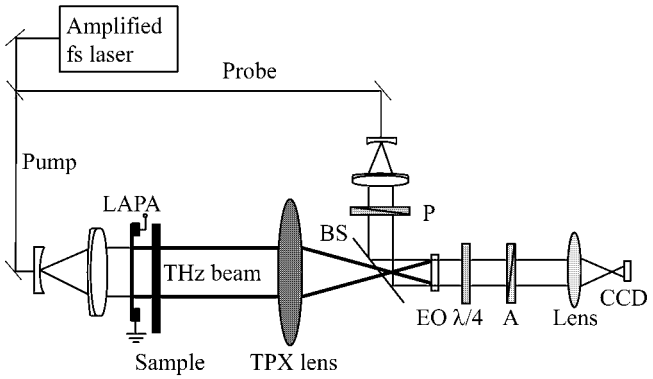

Figure 1. Schematic of a typical experimental setup of real-time THz imaging. LAPA: a large-aperture photoconductive antenna, BS: a pellicle beam splitter, EO: an electro-optic crystal (ZnTe), $\lambda/4$: a quarter-wave plate, P: a polarizer, A: a polarization analyzer.

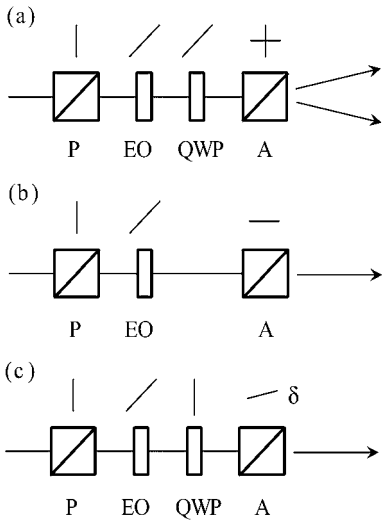

Figure 2. Configurations of optical elements used in the electro-optic sampling measurements. P: polarizer; EO: electro-optic crystal; QWP: quarter-wave plate; A: polarization analyzer. (a) Conventional EO sampling method. (b) THz intensity imaging. (c) THz field imaging.

spatial profile of the THz wave is measured by an EO sampling method using a spatially expanded probe pulse. In the EO sampling method, the birefringence induced in an EO crystal by the THz electric field is measured using a probe pulse. Because of the high intensity of the THz pulses, parallel two-dimensional measurement of the spatial profile is possible. In Fig. 2 are shown the configurations used in the measurements. In the conventional EO sampling method as shown in Fig. 2(a), balanced detection using two beams is carried out. In the two-dimensional measurements using an image detector, this method is difficult although not impossible. We adopted, therefore, a single-beam method. In the first method, which is shown in Fig. 2(b), two polarizers are placed perpendicular to each other. In this case, the signal intensity obtained is proportional to the square of the THz field, or the THz intensity. In the second method, which is shown in Fig. 2(c), we adopted the optical heterodyne detection method,[3] where we use a quarter-wave plate and orient the analyzer slightly off the perpendicular direction. In this case, the signal intensity has a term that is linearly proportional to the THz electric field, and field images can be calculated using the spatial distribution of the probe light intensity, I_0, the background intensity, I_b, and the signal intensity, I, as[3]

$$\theta = -\delta + \sqrt{\delta^2 + \frac{I - I_b}{I_0}}. \tag{1}$$

Here, δ is the orientation angle of the analyzer, θ is the retardation angle due to the EO effect, which is proportional to the THz field.

3. SPATIO-TEMPORAL PROFILES OF THZ PULSES

3.1. Temporal deformation

We have studied the change in the temporal waveforms of the THz pulses emitted from a large-aperture photoconductive antenna as a function of the propagation distance, and explained the results based on diffraction integral and Gaussian beam model. Detailed description of this study is given in a separate paper.[6] The emitter was a large-aperture antenna made of a semi-insulating GaAs wafer. Two electrodes were attached to the wafer, and the spacing between them was 30 mm. A pulsed voltage of 12 kV was applied to the electrodes. The emitter

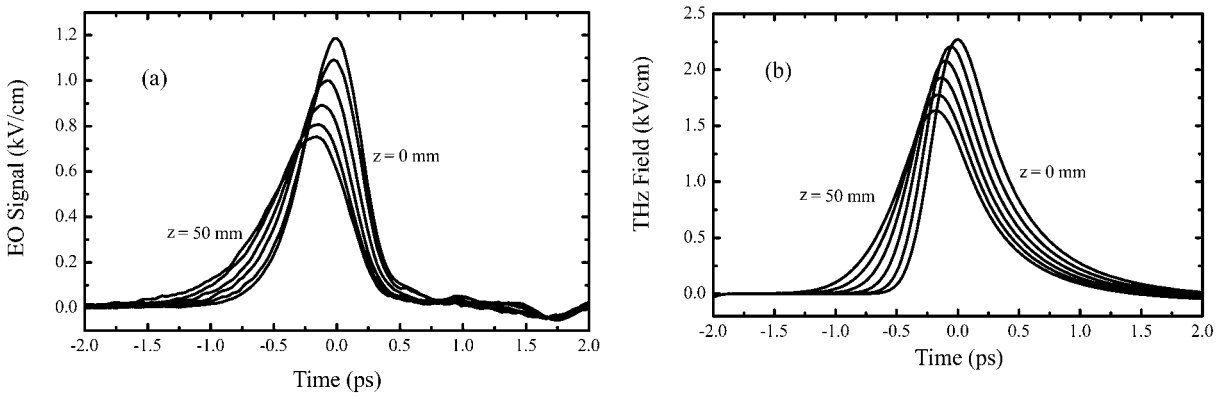

Figure 3. Temporal field waveforms of a focused THz pulse. The observation position was change from the focus ($z = 0$ mm) to 50 mm away from the focus ($z = 50$ mm) by a step of 10 mm. (a) Experimentally obtained data. (b) Calculated data obtained by simulation assuming Gaussian-beam propagation of each frequency component.

area between the electrodes was illuminated by amplified femtosecond optical pulses having 150-fs duration and 800-nm central wavelength. Charge carriers are created by the optical pulse radiation. They are accelerated by the applied electric bias field immediately after the creation, which leads to sudden change in the current at the surface of the wafer. The temporally changing current produces electric field. The process is described by a current surge model, and the expression for the surface field, $E_{\mathsf{surf}}(t)$, is given as

$$E_{\mathsf{surf}}(t) = -E_{\mathsf{bias}} \frac{\sigma_{\mathsf{s}}(t)\eta_0}{\sigma_{\mathsf{s}}(t)\eta_0 + 1 + \sqrt{\epsilon}}, \tag{2}$$

which shows that the field on the emitter surface is proportional to the current. Here, E_{bias} is the bias field, $\sigma_{\mathsf{s}}(t)$ is the time-dependent surface conductivity, ϵ is the dielectric constant of the emitter medium, and $\eta_0 = 377$ Ω is the impedance of vacuum. It has been shown, however, that the field at positions far from the surface is proportional to the time derivative of the surface field. The temporal waveform of focused THz pulses becomes proportional to the far field waveform as well:[6]

$$E_{\mathsf{focus}}(t) = \frac{A^2}{2cf} \frac{d}{dt} E_{\mathsf{surf}}(t). \tag{3}$$

Here, A is the beam size and f is the focal length. The time dependence of the surface current becomes step-like function with a fast rise when the lifetime of the carriers is sufficiently long, which results in a half-cycle shape of the far field waveform. These facts show that the THz pulse experiences drastic change in the temporal waveform during propagation and focusing in the free space.

In the experiments, we focused the THz pulses emitted from the large-aperture antenna using an off-axis parabolic mirror with a focal length of 152.4 mm. The position dependence of the temporal waveform of the electric field of the THz pulses was observed using an EO sampling method. Examples of the data obtained are shown in Fig. 3(a). All of the waveforms were observed on the propagation axis. We can see that the waveform is almost half-cycle at the focus, and is deformed significantly during the propagation. We simulated the waveform change using two methods. The first method uses the diffraction integral. This method can incorporate the actual shapes of the emitter and other components, but needs heavy calculation and the analysis of the results are sometimes not straightforward. The second one is based on the Gaussian beam model, where each frequency component of the THz pulse is assumed to propagate as a Gaussian beam. The results of the second method are shown in Fig. 3(b), which reproduced well the position dependence of the experimentally obtained waveform. Similar results were also obtained by the first method.

In a separate experiment,[7] we observed change in the temporal waveform of a THz field when the pulses are transmitted through a metal aperture. THz pulses are composed of a broad spectrum of frequency components. Each frequency component behaves in a different manner, which is evident in the position dependent

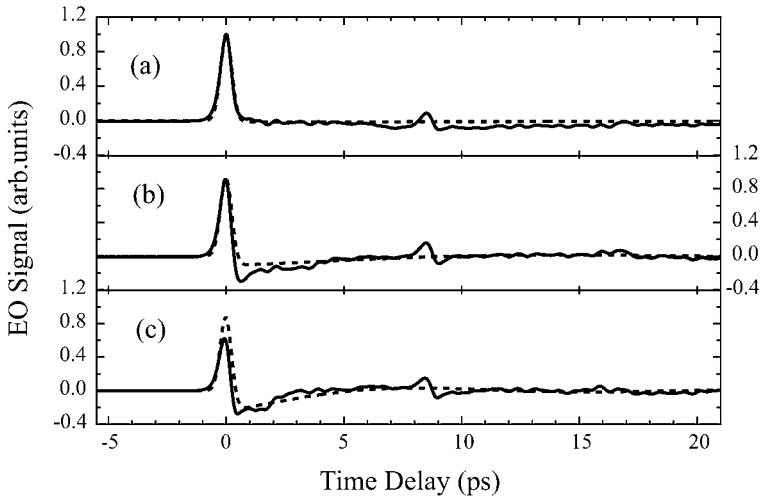

Figure 4. Waveforms of focused THz pulses that were passed through different sizes of circular metal apertures. Solid lines are the experimental results and the dotted lines are the simulated waveforms. (a) The waveform observed with only a 1-mm-thick 8-mm-size square aperture, which was used as a crystal holder cover, in front of the EO crystal. (b) and (c) The waveforms observed with a ϕ 3.8-mm and a ϕ 2.5-mm circular aperture in front of the EO crystal, respectively.

waveform described above. When THz pulses propagate through an aperture made of conductive materials, the frequency dependent propagation becomes more apparent because of the fact that conductive apertures behave as waveguides, which have a cutoff frequency:

$$\nu_{\mathrm{c}} = \frac{c}{2a}, \tag{4}$$

for a square waveguide with an edge length of a, and

$$\nu_{\mathrm{c}} = \frac{1.841}{2\pi} \cdot \frac{c}{r}, \tag{5}$$

for a circular waveguide with a radius of r. Here c is the velocity of light in vacuum. Components of frequency below the cutoff becomes evanescent and decays exponentially during the propagation through the aperture.

We observed the temporal waveforms of the THz pulses after propagation through a metal aperture at a position close to the aperture. The results are shown by the solid lines in Fig. 4. It is seen that a small dip is developed after the main peak in the THz waveforms due to the propagation through the aperture. The results were simulated using a simple model assuming the waveguide effect, as shown in the dotted lines in Fig. 4. These results show that relatively large apertures can affect the THz pulse waveforms significantly.

3.2. Spatial profiles

The pulses emitted from photoconductive antennas have very broad spectrum extending from dc to a few THz. Since the diffraction effects depend on the frequency, unique behaviors of spatial profile is observed with almost half-cycle THz pulses emitted from a large-aperture antenna. The spatial distribution of the THz wave was observed using a THz imaging setup with an expanded probe beam.[2,3] In Fig. 5(a)–(d) are shown the spatial distribution of the intensity of focused THz pulses on the focal plane at different times.[2] At $t = 0$ ps. which corresponds to the peak of the temporal waveform observed at the center, the spatial profile is smooth and has a single peak at the center. On the other hand, at negative and positive times, we observe ring-like profile. The observed behavior was reproduced by simulations using the diffraction integral, as shown in Fig. 5(e)–(h). It was shown that the appearance of the ring-like profile is unique for the half-cycle waveform of the pulses, and it can be explained by taking into account the frequency-dependent diffraction effects. Interestingly, similar behavior was also observed on the propagation distance dependence of the spatial profile,[2] as shown in Fig. 6. Knowledge on these behaviors are important for the implementation of real-time THz imaging.[4,5]

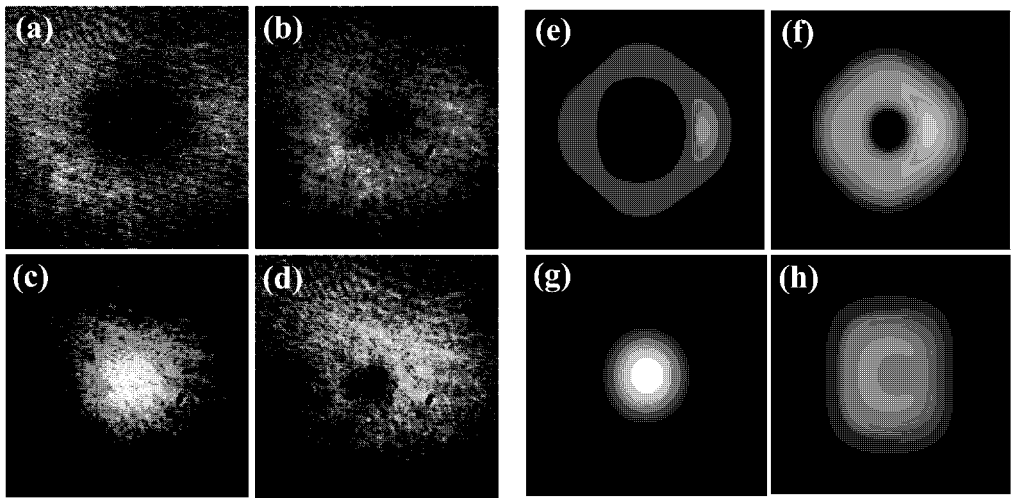

Figure 5. (a)–(d): Experimentally obtained intensity distribution of focused THz pulses on the focal plane at different times; (a) $t = -0.72$ ps, (b) $t = -0.48$ ps, (c) $t = 0$ ps, and (d) $t = 0.4$ ps. (e)–(h): THz intensity profiles obtained by simulation based on diffraction integral at times corresponding to those of (a)–(d), respectively. Each image corresponds to an area of 12×12 mm^2 at the EO crystal.

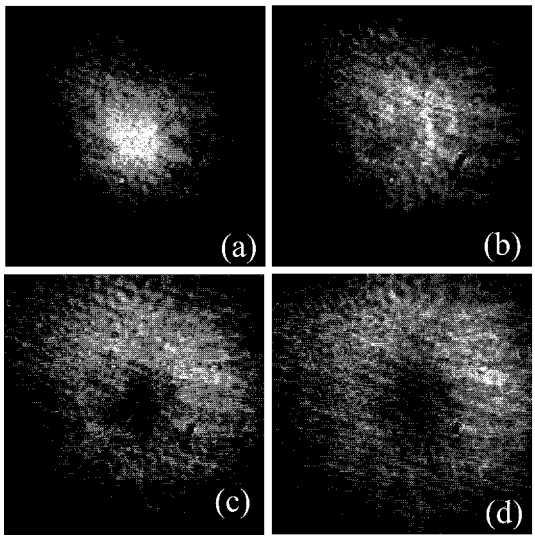

Figure 6. Experimentally obtained images of THz intensity distribution at a fixed delay time, $t = 0$ ps, on the plane at (a) $z = 0$ mm, (b) $z = 20$ mm, (c) $z = 40$ mm and (d) $z = 50$ mm.

Using the optical heterodyne detection technique which enables THz field imaging, frequency-resolved THz images can be obtained. For this purpose, field images were obtained while scanning the probe delay, and the temporal field waveform at each pixel was obtained by combining the image data. By Fourier transforming the waveforms and recombining specific frequency amplitudes, we obtained frequency-resolved THz images.[3]

In Fig. 7 are shown spatial distributions of the field amplitude of a focused THz pulse at specific frequencies. The figure shows that the higher-frequency components are more tightly focused. The observed beam sizes were almost proportional to the wavelength of the THz wave at each frequency. This is attributed to the diffraction limited focusing at each frequency component, and the observed results are consistent with the Gaussian beam theory. In performing THz imaging, the frequency-dependent diffraction plays an important role because the

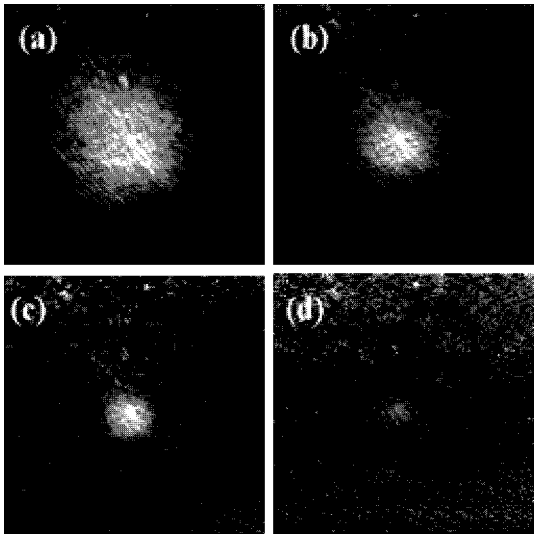

Figure 7. The spatial distribution of the electric field amplitude of (a) 0.48 THz, (b) 0.99 THz, (c) 1.50 THz and (d) 2.16 THz components of the focused THz pulse. The images correspond to an area of 18.2 mm × 18.2 mm at the position of the EO crystal. The amplitude is normalized to the peak value at each frequency. The peak value of image (d) is much smaller than that of (a), which enhances the relative level of the background noise of image (d).

spectrum of the THz pulses is very broad. On the other hand, the effects of aberration are much less significant in general.

4. HIGH-SPEED THZ IMAGING

Using intense THz pulses, two-dimensional EO sampling, and a high-speed image detector, high-speed THz imaging is possible. We succeeded in obtaining a THz image using only a single THz pulse, and also in obtaining a series of THz images of a moving object at a repetition rate of 1 kHz,[5] which is the repetition rate of the amplified laser output. By combining the images, high-speed movies of moving objects were obtained.

For this purpose, first we need to fix the time delay of the probe pulse of the EO sampling measurement at the time when we can obtain the clearest image. In Figs. 8 and 9, we show the temporal waveforms of the THz pulse on the propagation axis and THz images at several delay times. The experimental setup was similar to that shown in Fig. 1. The focal length of the TPX lens was $f = 98.3$ mm, and the distances from the sample object to the lens and from the lens to the EO crystal were $5f/2$ and $5f/3$, respectively. The waveform of the THz pulse at the focus (dotted line in Fig 8) is almost half-cycle and that on the image plane has a slow rise and a fast fall (solid line in Fig 8). THz images obtained at three delay times are shown in Fig. 9. The sample was a metal rod of 2 mm in diameter concealed in a paper box. Images (a) and (b) were obtained at the time corresponding to the peak of the on-axis THz waveform ($t = 0$ ps). Images (c) and (d) were obtained at $t = 0.7$ ps, where the waveform has the largest change rate. Images (e) and (f) were obtained at $t = 1.0$ ps, where the THz field is negative. Images in the left column ((a), (c), and (e)) were obtained by subtracting a reference image, which was acquired with no sample object, from the raw images. Images in the right column ((b), (d), and (f)) were obtained by dividing the raw image data by the reference image data. From these images, we see that the image quality depends very much on the observation time, and that the best images are obtained at the time when the on-axis THz waveform has the largest temporal change. This result can be explained as follows. At the peak time ($t = 0$ ps), the THz field is the largest, but the major contribution is from low-frequency components. This leads to the low spatial resolution observed in images (a) and (b). At the time when the temporal change in the THz field is largest ($t = 0.7$ ps), amplitudes of higher-frequency components become largest, which results in the best quality and the highest resolution of images, as seen in images (c) and (d), which reproduce the shape of the sample object well. At the time when the THz field has fallen to a negative value ($t = 1.0$ ps), the spatial

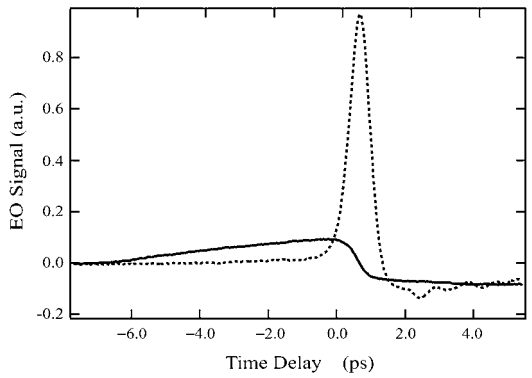

Figure 8. On-axis temporal waveforms of the THz pulses on the focal plane, $z = f$, (dotted line) and on the image plane, $z = 5/3f$, (solid line) measured using the conventional balanced detection method.

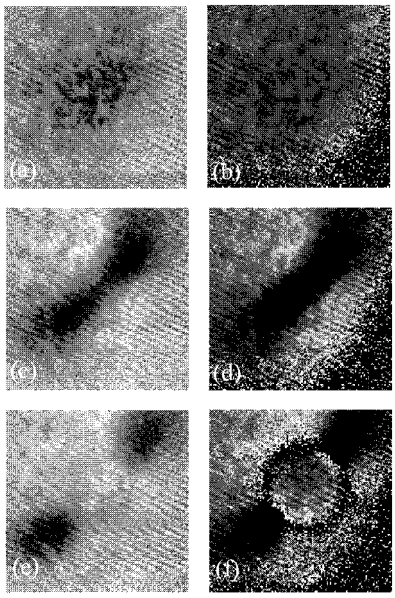

Figure 9. Left column: difference images; obtained by subtracting the reference image data from the sample image data at respective delay times. Right column: division images; obtained by dividing the sample image data by the reference image data. Images (a) and (b) were obtained at the peak time (0 ps) of the THz field. Images (c) and (d) were obtained at 0.7 ps, and (e) and (f) at 1.0 ps.

profile of the THz field exhibits the ring-like structure, as described in Sect. 3, which leads to the circular artifact structure in the images, as seen in (e) and (f).

By fixing the delay time of the probe pulse in the best time window, we obtained a high-speed THz movie of a moving object at a frame rate of 1,000 frame/s. The sample object was a metal rod hung by a string in front of the THz emitter. Real-time images of the rod, while swinging, were obtained using a high-speed CCD camera. The camera can capture images at a repetition rate of 1 kHz. The laser amplifier, the high voltage supply to the THz emitter, and the CCD camera were synchronized to an external clock at 1 kHz. Each image was obtained using only a single THz pulse.

Examples of the obtained single-shot THz images are shown in Fig. 10. Images (a) and (b) were obtained by dividing the sample images by the reference image. Image (b) were obtained 20 ms after image (a). It is seen that the signal-to-noise ratio is quite low in these images because of the single-shot detection. In order to reduce the noises, we applied a Gaussian filter to these images, which reduces amplitudes of high-spatial-frequency components in the image, and obtained images (c) and (d), which clearly show the shape and the position change of the metal rod.

We obtained a 1,000-frame/s high-speed movie of the swinging metal rod by applying the Gaussian filter to each image and combining them together. The calculation of the Gaussian filtering took 0.5 s per a frame on a personal computer. Snapshots of them are shown in Fig. 11, which clearly show the movement of the metal rod from left to right.

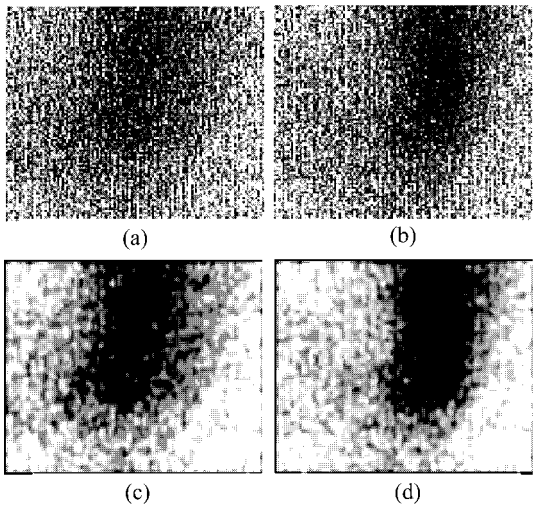

Figure 10. Shadow of a metal rod detected by a single THz pulse (a) and (b); obtained by dividing the sample image data (with the rod) by the reference image data (without the rod). The image (b) was obtained 20 ms after image (a). Images (c) and (d) are the results of applying a Gaussian filter operation to images (a) and (b), respectively. The images correspond to dimension of 8.8×7.4 mm^2 on the object plane.

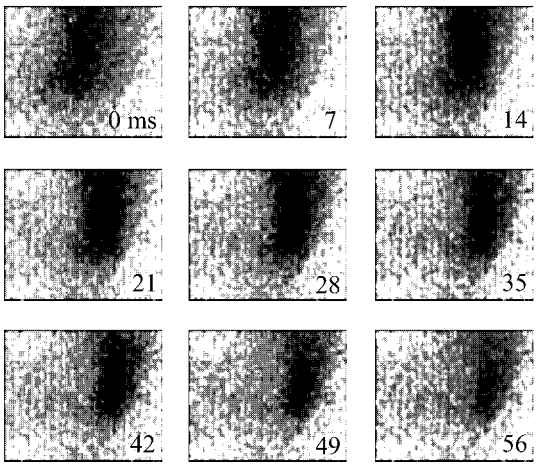

Figure 11. Snapshots of a movie showing the translation of a metal rod from left to right with a time interval of 7 ms. The original movie has a frame rate of 1,000 frames/s, and each image was obtained using a single THz pulse. The images correspond to dimension of 8.8×7.4 mm^2.

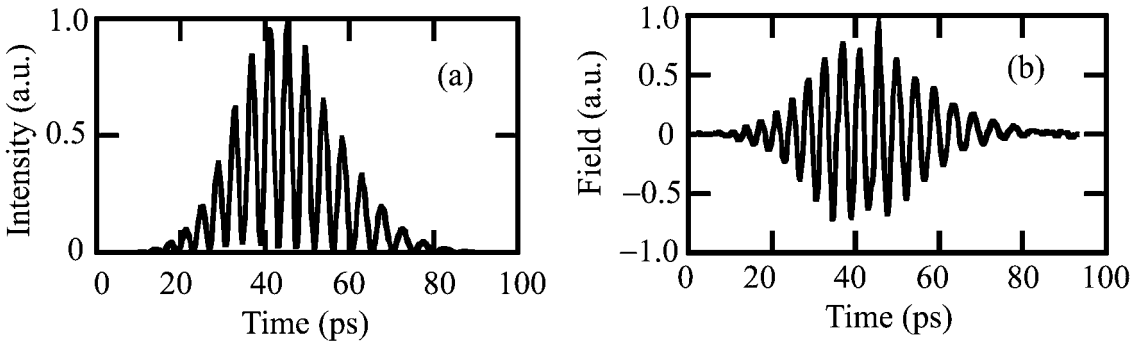

Figure 12. (a) An example of a temporal waveform of the intensity-modulated laser pulses obtained by a second-harmonic-generation cross-correlation method. (b) Temporal waveform of the tunable phase-stable THz pulse generated using the optical pulse shown in (a), which was measured using an EO sampling method.

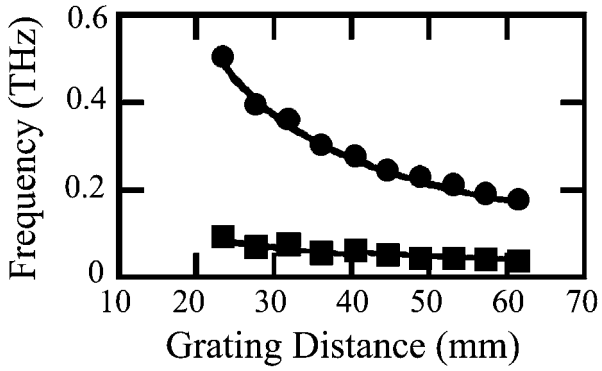

Figure 13. Grating distance dependence of the center frequency (circles) and bandwidth (squares) of the tunable THz pulses.

5. TUNABLE NARROW-BAND THZ PULSE GENERATION

Instead of half-cycle THz pulses, narrow-band pulses are suitable for some applications such as coherent control, spectroscopy, and communications. Tunable picosecond THz pulses have been generated by Weling and Auston[9] using interference between two linearly chirped optical pulses. We applied a novel technique for creating a pair of pulses in this method, and obtained phase-stable tunable THz pulses.

In the experiment, a photoconductive antenna was excited by optical pulses having a sinusoidal intensity modulation, which was obtained from beating of an interferenced time-delayed pair of linearly-chirped femtosecond pulses. In the conventional method, the linearly-chirped pulses are obtained using a pair of a grating, and the pulse pair using a Michelson interferometer. The beating frequency f_0, which is also the center frequency of the emitted THz pulses, and the THz bandwidth Δf are expressed as

$$f_0 = \frac{\mu\tau}{2\pi} \tag{6}$$

and

$$\Delta f = \frac{\sqrt{2}\sigma\mu}{\pi}, \tag{7}$$

respectively.[9] Here, μ is a parameter related to the linear chirp, τ is the delay time between the pulse pair, and σ is the duration of the unchirped pulse.

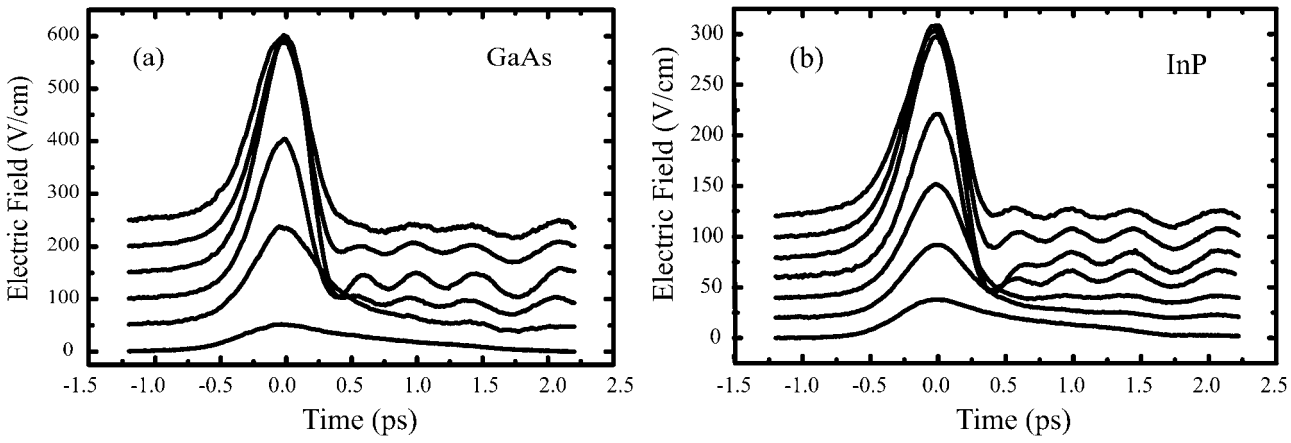

Figure 14. Temporal waveforms of the THz pulses emitted from (a) GaAs and (b) InP for several values of the excess pump photon energy with respect to the band gap energy. The bias electric field applied to the emitter material was kept at 6.7 kV/cm. In (a), waveforms are shown for excess energies of −35, −19, −3, 14, 66, and 122 meV from the bottom to the top. Each plot is shifted upward by 50 kV/cm. In (b), waveforms are shown for excess energies of −46, −32, −18, −3, 11, 108, and 198 meV from the bottom to the top. Each plot is shifted upward by 20 kV/cm. Oscillations observed in waveforms at positive excess energies are due to water vapor absorption and will not be discussed in the text.

We used a birefringent crystal instead of the interferometer to generate the pulse pair. Since the time delay between the pulse pair is related not only to the carrier frequency of the THz pulses, but also to the phase of the THz field oscillation, we can obtain a stable carrier-envelope phase of the THz pulses by using a birefringent crystal instead of an interferometer. Furthermore, the optical setup can be much more compact. Examples of generated pulse waveforms are shown in Fig. 12. Figure 12(a) shows a waveform of the intensity-modulated optical excitation pulse, and Fig. 12(b) shows that of the emitted THz pulse. By varying the distance between the grating pair, the chirping rate of the optical pulse can be changed. The grating distance dependences of the center frequency and the bandwidth of the emitted THz pulses are plotted in Fig. 13, which are consistent with Eqs. 6 and 7. As seen from the equations and the figure, the center frequency and the bandwidth are proportional to each other in the present scheme when an identical birefringent crystal is used.

6. ULTRAFAST SEMICONDUCTOR SPECTROSCOPY

THz radiation emitted from photoconductive antennas can be used for the study of the ultrafast dynamics of carriers in the emitter materials. The large-aperture structure of the emitter is especially suited for the dynamics study since the emitted THz waves have a clean wavefront, and the carrier dynamics is not affected by the emitter structure. We observed the temporal waveforms of the THz pulses emitted from a large-aperture antenna made of GaAs and InP by varying the excitation photon energy.[8] We used an optical parametric amplifier to change the wavelength of the excitation pulses, and band-pass filters to limit the bandwidth to 10 nm. The THz waveforms observed are plotted in Fig. 14 for several excess energies, which are defined by the excitation photon energies minus the bandgap energy of each material. At positive excess energies, the observed peak THz field is slightly decreased and the THz pulses width is slightly increased for larger excess energies. This tendency is due to the excess energy dependence of the thermalization dynamics of the electrons within the conduction band, which occurs within 1 ps after the photoexcitation. At negative excess energies, on the other hand, we observe an exponentially decaying tail in the THz waveforms with a time constant of 1–2 ps. We attribute this to a slow rise in the mobility of electrons due to a transition of electrons from an initial unmobile state, which is created by excitation in the Urbach tail region, to a more mobile free-carrier state. We also found that the decay times depend on the applied bias field very sensitively, as shown in Fig. 15,

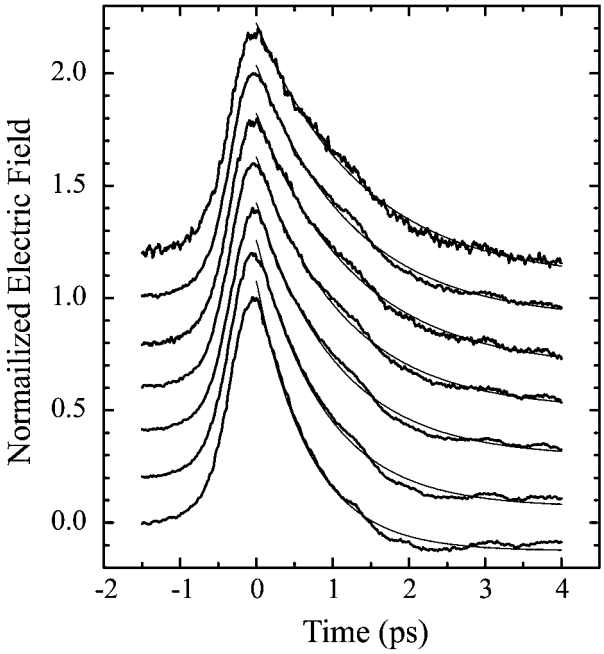

Figure 15. Thick lines show the bias field dependence of the temporal waveforms of the THz pulses emitted from GaAs pumped with an excess energy of −35 meV. The values of the bias field are 1.3, 2.7, 4.0, 5.3, 6.7, 8.0, and 9.3 kV/cm from the top to the bottom. Thin lines show the fit of the decaying part to an exponential function.

7. CONCLUSION

We generated intense THz pulses using a large-aperture photoconductive antenna, and applied the pulses to real-time THz imaging and ultrafast spectroscopies. The temporal waveform obtained was almost half-cycle at the focus, and waveform change near the focus was explained using the Gaussian beam model. The spatio-temporal profiles of the THz pulses exhibited ring-like spatial structure, which was simulated using the diffraction integral. High-speed THz movies of a moving object at a frame rate of 1,000 frames/s were obtained by single-shot THz image acquisition at a repetition rate of 1 kHz. Time-domain THz emission spectroscopy of GaAs and InP revealed the ultrafast electron dynamics at excitation energies above and below the bandgap.

REFERENCES

1. T. Hattori, K. Tukamoto, and H. Nakatsuka, "Time-resolved study of intense terahertz pulses generated by a large-aperture photoconductive antenna," Jpn. J. Appl. Phys. 40, pp. 4907–4912 (2001).
2. R. Rungsawang, K. Ohta, K. Tukamoto, and T. Hattori, "Ring formation of focused half-cycle terahertz pulses," J. Phys. D 36, pp. 229–235 (2003).
3. T. Hattori, K. Ohta, R. Rungsawang, and K. Tukamoto, "Phase-sensitive high-speed THz imaging," J. Phys. D 37, pp. 770–773 (2004).
4. R. Rungsawang, K. Tukamoto, and T. Hattori, "Electric field imaging using intense half-cycle terahertz pulses," Jpn. J. Appl. Phys. in press.
5. R. Rungsawang, A. Mochiduki, S. Ookuma, and T. Hattori, "1-kHz real-time imaging using a half-cycle electric pulse," submitted to Jpn. J. Appl. Phys.
6. T. Hattori, R. Rungsawang, K. Ohta, and K. Tukamoto, "Gaussian beam analysis of temporal waveform of focused terahertz pulses," Jpn. J. Appl. Phys. 41, pp. 5198–5204 (2002).
7. K. Tukamoto, R. Rungsawang, and T. Hattori, "Propagation of focused terahertz pulses through subcentimeter conductive apertures," Jpn. J. Appl. Phys. 42, pp. 1609–1613 (2003).

8. T. Hattori, S. Arai, and K. Tukamoto, "Ultrafast electron dynamics in GaAs and InP studied by time-resolved terahertz emission spectroscopy," Jpn. J. Appl. Phys. 43, pp. 7546–7551 (2004).
9. A.S. Weling and D.H. Auston, "Novel sources and detectors for coherent tunable narrow-band terahertz radiation in free space," J. Opt. Soc. Am. B 13, pp. 2783–2791 (1996).